Promoting TOD through regional planning. A comparative analysis of two European approaches

ADVANCED MATERIALS TECHNOLOGIES
www.advmattechnol.de

Autodrop-Enabled Aqueous Deposition of $BiVO_4$–$FePO_4$ Photoanodes for Stable Water Splitting

Roberto Altieri, Matteo Crisci, Derck Schlettwein, Bernd Smarsly, Francesco Lamberti, Teresa Gatti, and Mengjiao Wang**

Scalable and sustainable methods for fabricating stable photoelectrodes are essential for advancing solar-driven water splitting. Here, an automated aqueous deposition approach is demonstrated, which is named "Autodrop", for the fabrication of $BiVO_4$–$FePO_4$ photoanodes via a modified successive ion layer adsorption and reaction (SILAR) process. The method enables precise control over film thickness and morphology using low-toxicity precursors and ambient conditions. The integration of an amorphous $FePO_4$ layer on top of the $BiVO_4$ photo-absorber serves as both a passivation coating and co-catalyst, resulting in a 50% photocurrent increase and excellent operational stability, with over 80% of the initial current retained after 2 h of continuous chronoamperometry under AM 1.5G illumination at 1.23 V versus RHE. These results establish Autodrop as a versatile platform for scalable, multi-layer photoelectrode fabrication, supporting the development of next-generation PEC devices.

1. Introduction

The intermittent nature of solar and wind power demands efficient strategies for energy storage and conversion.[1,2] Among these, hydrogen production via photoelectrochemical (PEC) water splitting is a promising approach for delivering renewable, CO_2-free fuels.[3] However, the anodic oxygen evolution reaction (OER) remains a key bottleneck, requiring robust and efficient photoanode materials.[4–6] $BiVO_4$is one of the most studied photoanode materials for OER due to its suitable band gap of 2.4–2.6 eV and a theoretical maximum photocurrent density of ≈7.5 mA cm^{-2}.[7] Moreover, $BiVO_4$ offers superior hole conductivity, with a hole mobility of 2 $cm^2\ V^{-1}s^{-1}$, which is significantly higher than that of the widely used Fe_2O_3 photoanode (10^{-4} $cm^2\ V^{-1}s^{-1}$).[8] Additionally, $BiVO_4$ is cost-effective and non-toxic, making it a promising candidate for PEC applications. However, its performance is hindered by a short hole diffusion length (70 nm), low electron mobility (0.02–0.044 $cm^2\ V^{-1}s^{-1}$), and a limited carrier lifetime (40 ns).[9,10] Furthermore, one of its major challenges is photo-corrosion over time, primarily due to the loss of V ions in aqueous solutions.[9] These challenges can be mitigated by thin-film engineering and the integration of passivation layers that enhance charge separation and surface stability.

The use of protective materials is a well-established strategy for improving the stability of photoelectrocatalysts. Inert oxides such as ZnO, TiO_2, and Al_2O_3 have been employed as passivation layers for photoanodes.[11,12] For example, Al_2O_3 helps inhibit surface recombination on $BiVO_4$.[11] A thin TiO_2 passivation layer can double the photocurrent of $BiVO_4$/CuO by preventing photogenerated holes in CuO from transferring into the electrolyte.[13] Additionally, the photocurrent density of ZnO/TiO_2–coated $BiVO_4$ is 2.5 times higher than that of pristine $BiVO_4$.[14] However, their deposition typically requires advanced techniques like atomic layer deposition, which can be complex and costly. Li Z. and coworkers showed that it is also possible to have an increase in photocurrent with a thin TiO_x overlayer via drop-casting and O_2 plasma treatment on WO_3 photoanodes.[15] Alternatively, $FePO_4$ has been identified as an effective passivation layer for Fe_2O_3 and $BiVO_4$ photoanodes, with successful coatings achieved through liquid-phase deposition.[16,17]

R. Altieri, M. Crisci, D. Schlettwein, B. Smarsly, T. Gatti
Center for Materials Research
Justus Liebig University
Heinrich-Buff-Ring 17, 35392 Giessen, Germany
E-mail: teresa.gatti@polito.it
R. Altieri, M. Crisci, B. Smarsly
Institute of Physical Chemistry
Justus Liebig University
Heinrich-Buff-Ring 17, 35392 Giessen, Germany
D. Schlettwein
Institute of Applied Physics
Justus Liebig University
Heinrich-Buff-Ring 16, 35392 Giessen, Germany
F. Lamberti
Dipartimento di Scienze Chimiche
Università degli Studi di Padova
Via Marzolo, 1, Padova 35131, Italy
T. Gatti, M. Wang
Department of Applied Science and Technology
Politecnico di Torino
Corso Duca degli Abruzzi 24, Torino 10129, Italy
E-mail: mengjiao.wang@polito.it

The ORCID identification number(s) for the author(s) of this article can be found under https://doi.org/10.1002/admt.202500672

DOI: 10.1002/admt.202500672

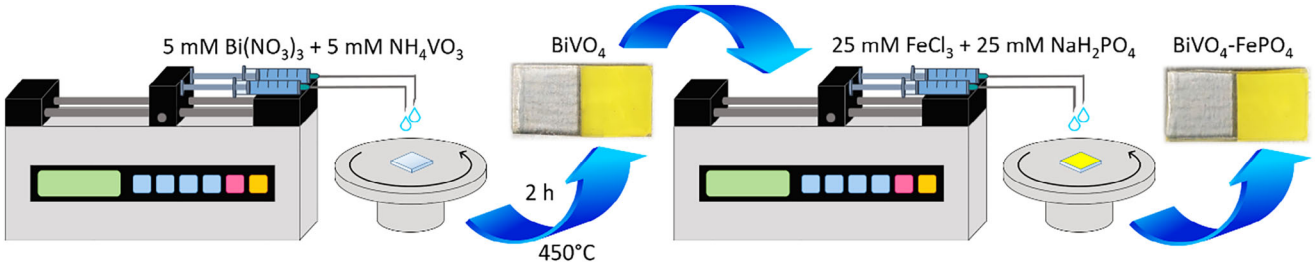

Figure 1. Schematic representation of the AutoDrop process developed in this work to produce $BiVO_4$–$FePO_4$ sustainable photoanodes.

Due to its synthesis mechanism, $FePO_4$ can feasibly be grown on $BiVO_4$ films using different methods, providing a straightforward and efficient approach to enhancing photoanode stability.

The fabrication of thin films of photoactive materials is essential for optimizing their optical and electronic properties, ultimately enhancing photoelectrocatalytic performance. Synthesizing $BiVO_4$ as a thin film effectively mitigates its intrinsic challenges, including short carrier diffusion length, rapid charge recombination, and photo-corrosion.[18] This strategy improves charge separation and transport, leading to higher photocurrent densities. Several synthesis methods are available for $BiVO_4$ thin films, including drop casting,[19] hydrothermal processing, electrodeposition, successive ion layer adsorption and reaction (SILAR), and sol-gel techniques.[20] Among these strategies for $BiVO_4$ thin films, SILAR stands out for its simplicity, scalability, and low-temperature aqueous processing.[21] Recent studies have shown that film morphology, thickness, and crystallinity can be tuned via SILAR to significantly affect PEC performance.[22,23] This method is particularly suitable for $BiVO_4$ as it enables the formation of uniform nanoporous films while allowing precise control over deposition cycles to enhance PEC performance. Furthermore, SILAR is easily automated, making it a promising technique for scalable synthesis and industrial applications. Our group has recently demonstrated an automated version of SILAR ("Autodrop") for BiOI photoelectrodes.[24] This version integrates a dual syringe pump for continuous precursor solution delivery and a spin coater to enhance film uniformity. These improvements streamline the deposition process, making it more controllable and efficient than conventional SILAR methods, thereby enhancing scalability for thin film production.

Building on our previous work with the automated SILAR technique for BiOI-based photoanodes, this study represents the first application of the Autodrop method to both $BiVO_4$ and a complex $BiVO_4$–$FePO_4$ heterostructure. Unlike standard SILAR, Autodrop combines spin-assisted deposition with continuous precursor delivery via a dual-syringe pump, offering programmable control over timing, flow rate, and precursor volume. This allows for precise tuning of film morphology and composition, distinguishing it from conventional drop-casting, which suffers from poor uniformity and limited reproducibility. We systematically investigate how Autodrop parameters (dropping rate, spinning speed, dropped volume) influence $BiVO_4$ film quality and PEC performance. Notably, $BiVO_4$ films fabricated by Autodrop form directly on the substrate surface with improved nanostructuring and uniformity, enabling superior PEC activity compared to drop-cast films. Furthermore, a secondary $FePO_4$ layer is deposited via Autodrop in a two-step process to enhance OER performance and stability. This configuration results in a 50% photocurrent increase and >80% retention over 2 h at 1.23 V versus RHE. This work demonstrates not only the material-level advantages of Autodrop but also its scalability and suitability for automation, bridging the gap between laboratory-scale synthesis and industrially viable electrode fabrication. Autodrop reduces fabrication time, operates under ambient conditions, and enables systematic optimization–positioning it as a novel, generalizable method for the sustainable and automated fabrication of high-performance photoelectrodes.

2. Results and Discussion

2.1. Structural and Morphological Characterization

The samples were fabricated using the Autodrop setup, as illustrated in **Figure 1** (see Experimental Section for details). The experiment was designed using the control variable method, where one key parameter—dropping rate (typically 100 µL min^{-1}), spinning speed (typically 40 rps), or total dropped volume (typically 2.0 mL)—was systematically varied while keeping the other two constant at the typical value. This experimental design of experiment allows for a precise evaluation of how each parameter individually influences film formation. A comprehensive list of parameter combinations is provided in Table S1 (Supporting Information). The $BiVO_4$ thin films were deposited on fluorine-doped tin oxide (FTO) glass substrates using the Autodrop method and subsequently annealed at 450 °C. The annealed samples were then subjected to further characterization. The phase composition of the $BiVO_4$ films was analyzed via X-ray diffraction (XRD). As the dropped volume increased while keeping other parameters constant, a pure $BiVO_4$ monoclinic scheelite phase (ICSD 100602) was observed, accompanied by a broadening of the main reflection at 29° in the XRD pattern (**Figure 2a**). The average crystallite size of $BiVO_4$, calculated using the Scherrer equation, increased from 15 to 18 nm as the drop volume increased from 0.5 to 3 mL (Figure 2b). Varying the spinning speed did not significantly affect the phase composition or particle size, as shown in Figure 2c and Figure S1a (Supporting Information). Meanwhile, XRD analysis of films synthesized at different dropping rates (Figure 2d) confirmed that most samples exhibited the monoclinic scheelite phase, except for the sample deposited at 25 µL min^{-1}. This sample contained a mixture of $BiVO_4$, Bi_2O_3 (ICSD 420602), and V_2O_5 (ICSD 43132). This suggests that when the dropping rate is too slow (<25 µL min^{-1}), the precursor

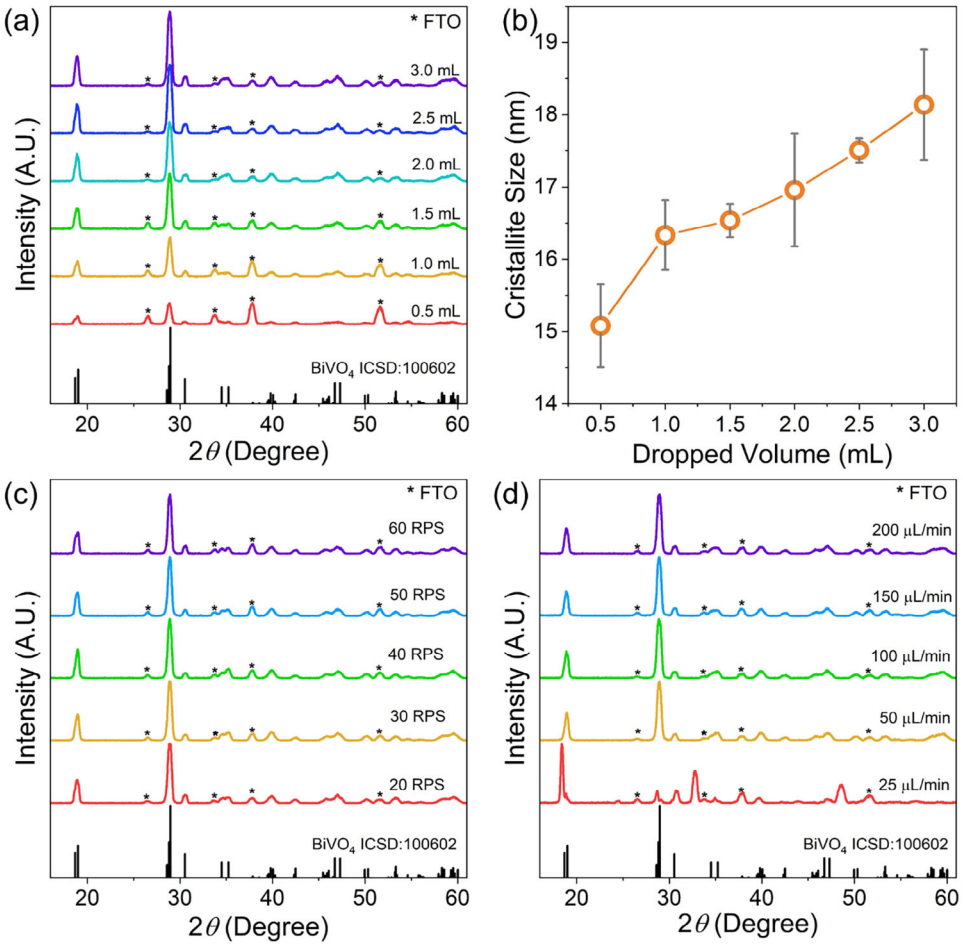

Figure 2. XRD patterns of $BiVO_4$ thin films prepared by Autodrop with varying parameters, namely by changing, a) the dropped volume at 100 µL min^{-1} and 40 rps, c) the spinning speed at 100 µL min^{-1} and 2.0 mL, and d) the dropping rate at 40 rps and 2.0 mL. b) Crystallite sizes were calculated using the Scherrer equation from diffractograms in Figure 2a.

solutions tend to form Bi_2O_3 and V_2O_5 separately, rather than reacting appropriately to achieve the desired $BiVO_4$ stoichiometry, leading to the formation of secondary crystalline phases after annealing. Regarding the particle size, the dropping rate appeared to have minimal impact, with all samples exhibiting particle sizes in the range of 17–18 nm (Figure S1b, Supporting Information).

To examine the impact of Autodrop parameters on the morphology of $BiVO_4$, scanning electron microscopy (SEM) images are presented in **Figure 3**. As the dropped volume of the precursor solution increases (Figure 3a–f), a higher density of nanostructure agglomerations is observed. In the first sample (Figure 3a), where each precursor solution volume is 0.5 mL, the nanostructure remains relatively dispersed. However, in subsequent samples (Figure 3b–f), as the precursor volume increases, the particles become more closely packed and continue to grow atop one another. Additionally, an increase in nanostructure domain size is evident with higher total dropped volume. The film thickness is also significantly affected by the dropped volume, as shown in Figure 3a–f, with $BiVO_4$ films exhibiting a porous structure composed of clustered nanostructures. The thickness increases from ≈300–400 nm at 0.5 mL to ≈1.7 µm at 3.0 mL. In contrast, increasing the spinning speed (Figure S2a–e, Supporting Information) appears to promote the formation of larger clusters. While these morphological changes do not directly align with the crystallite size determined using the Scherrer equation, this discrepancy is expected. The Scherrer equation estimates the size of individual crystallites, whereas SEM images capture the size of aggregated clusters. Furthermore, increasing the dropping rate (Figure 3g–j) leads to the formation of larger and more densely packed structures. Given that the crystallite size calculated from XRD remains relatively unchanged, it is likely that small crystallites form initially and later aggregate into larger structures.

2.2. Optical Characterization

To evaluate how the Autodrop parameters influence the optical properties of $BiVO_4$ films, UV–vis diffuse reflectance spectroscopy was conducted using an integrating sphere. All samples display a characteristic absorption in the 400–650 nm range, consistent with the semiconducting nature of $BiVO_4$. Variations in dropped volume, spinning speed, and dropping rate were

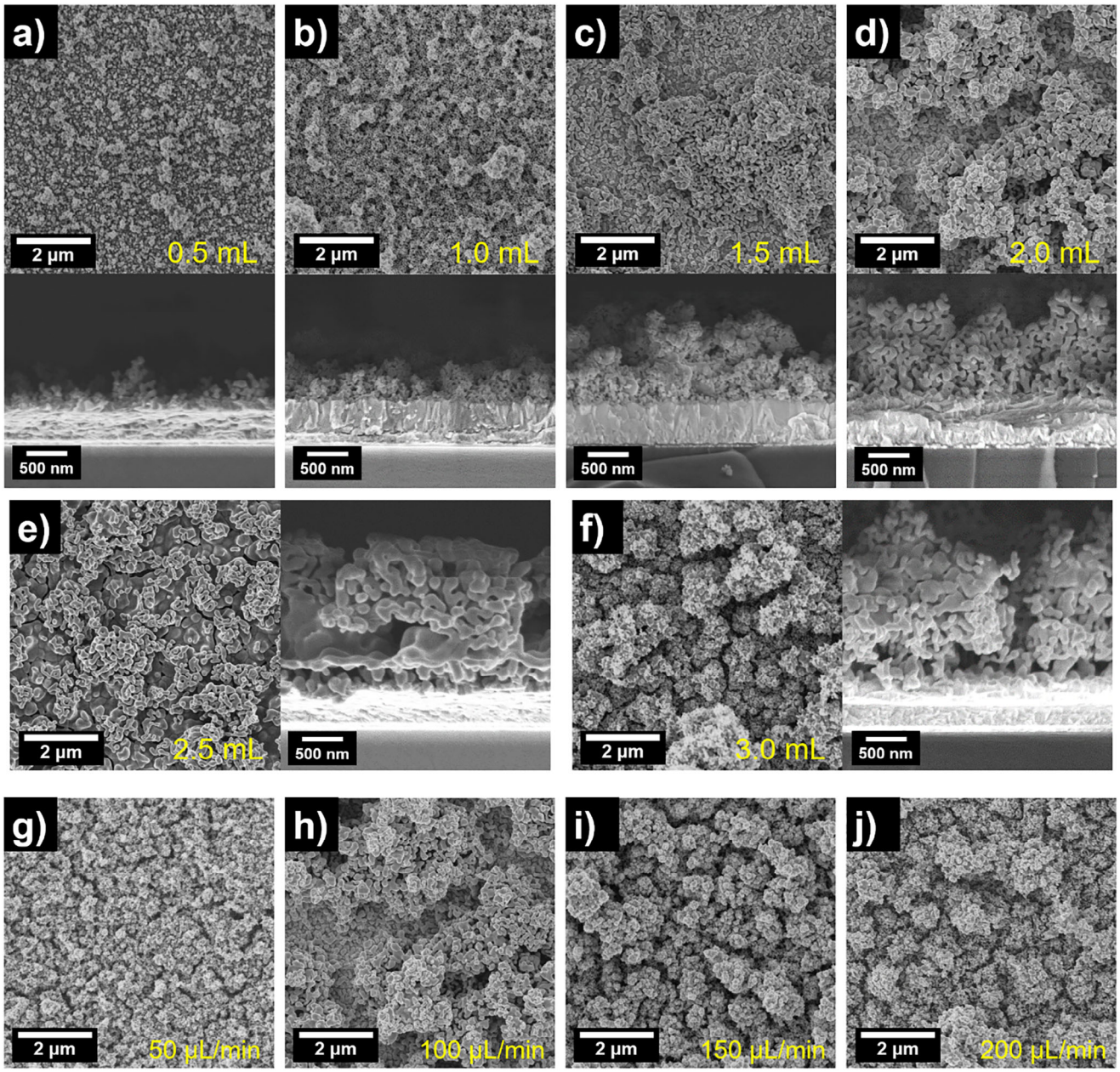

Figure 3. SEM images of $BiVO_4$ samples prepared by Autodrop at varying deposition parameters. Top view and cross-section of $BiVO_4$ samples prepared increasing dropped volume at 100 µL min^{-1} and 40 rps: a) 0.5 mL; b) 1.0 mL; c) 1.5 mL; d) 2.0 mL; e) 2.5 mL; f) 3.0 mL. Samples prepared with different dropping rates at 40 rps and 2.0 mL, g) 50 µL min^{-1}, h) 100 µL min^{-1}, i) 150 µL min^{-1}, j) 200 µL min^{-1}.

systematically analyzed to assess their impact on the band structure and optical transitions. The original UV–vis spectra are shown in Figure S3 (Supporting Information). It is evident that the absorption of the samples increases with the drop volume, likely due to the corresponding increase in film thickness, as observed in Figure 3. In contrast, variations in spinning rate have a much smaller effect on absorption, although the sample prepared at 20 rps shows slightly higher absorption. Overall, the dropping rate appears to have a minor influence compared to the drop volume. For comparison, the spectra from Figure S3 (Supporting Information) are normalized and presented in **Figure 4**. As shown in Figure 4a–c, an increase in dropped volume leads to a gradual bandgap reduction (calculated by Tauc plot) from ≈2.7 to 2.52 eV as the volume increases from 0.5 to 3 mL. This trend aligns with the observations of Ratnayake et al., who reported that a lower bandgap is associated with a greater number of SILAR cycles due to an increase in crystallite size, as confirmed by XRD analysis (Figure 2a).[23] Similarly, in the Autodrop process, films deposited with smaller drop volumes exhibit a slightly higher bandgap. Adjusting the spinning speed also influences the bandgap, as shown in Figure 4d–f. When the spinning speed increases from 20 to 60 rpm, the bandgap rises from 2.53 to 2.60 eV. This effect may

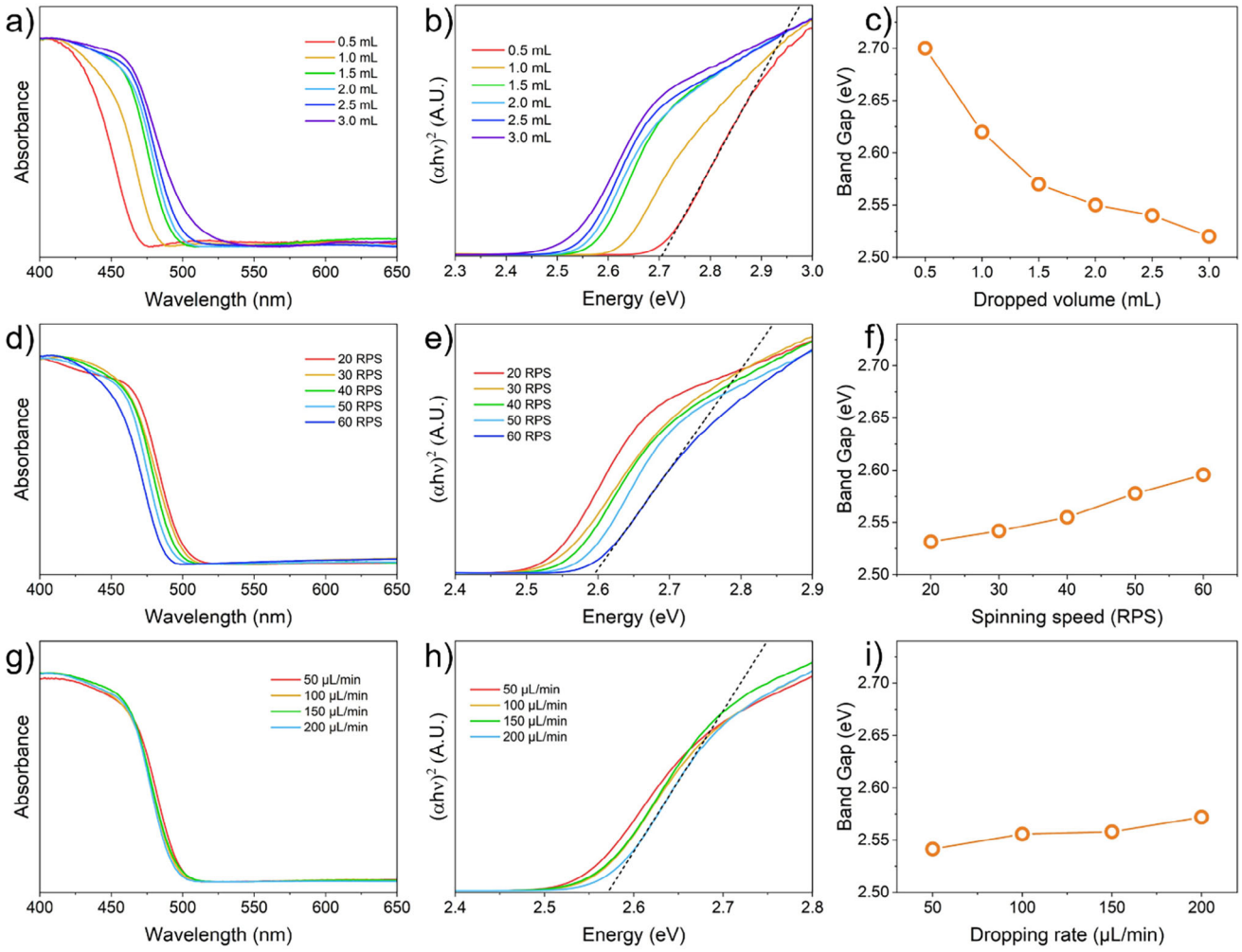

Figure 4. Normalized UV–vis absorption spectrum of $BiVO_4$ thin films changing: a) the dropped volume at 100 µL min^{-1} and 40 rps, d) the spinning speed at 100 µL min^{-1} and 2.0 mL, and (g) the dropping rate at 40 rps and 2.0 mL. Tauc plots in (b), (e), and (h) were obtained from graphs (a), (d), and (g), respectively. c), (f) and (i) are trends in bandgap values obtained from graphs (b), (e), and (h), respectively.

result from the formation of thinner films at higher spinning speeds, leading to a broader bandgap. Additionally, the effect of varying the dropping rate is illustrated in Figure 4g–i. As the dropping rate increases from 50 to 200 µL min^{-1}, the bandgap slightly increases from 2.54 to 2.58 eV. These findings indicate that the dropping rate has a relatively minor effect on the bandgap compared to other parameters.

2.3. Surface Characterization

The surface composition of the material was examined using X-ray photoelectron spectroscopy (XPS) on a typical $BiVO_4$ film. The presence of Bi, V, and O was confirmed, as shown in **Figure 5**, with a representative survey spectrum provided in Figure S4a–4b (Supporting Information). In the Bi 4f region, two distinct peaks were observed at binding energies of 164.4 and 159.2 eV, corresponding to the Bi $4f_{5/2}$ and Bi $4f_{7/2}$ core levels, respectively (Figure 5a). The spin-orbit splitting of 5.2 eV confirms that Bi is in the +3 oxidation state within an oxide environment.[25] Similarly, the characteristic peaks of V were identified at 524.3 eV (V $2p_{1/2}$) and 516.7 eV (V $2p_{3/2}$), verifying the presence of vanadium in the +5 oxidation state (Figure 5b). The O 1s spectrum displayed a primary peak centered at 529.8 eV, attributed to lattice oxygen in $BiVO_4$ (Figure 5c, blue area). Additionally, a higher binding energy shoulder at ≈531.2 eV was observed, likely corresponding to hydroxide species. Overall, the XPS analysis confirms the presence of $BiVO_4$ on the surface, with no detectable impurities, proving the high quality of the Autodrop fabrication method for the photonaodes.[22,23]

2.4. Photoelectrochemical Characterization of $BiVO_4$ Photoanodes

The $BiVO_4$ samples were evaluated for their performance in the photoelectrocatalytic water oxidation reaction. Testing was conducted in a 0.5 M Na_2SO_4 aqueous solution at pH 7 under

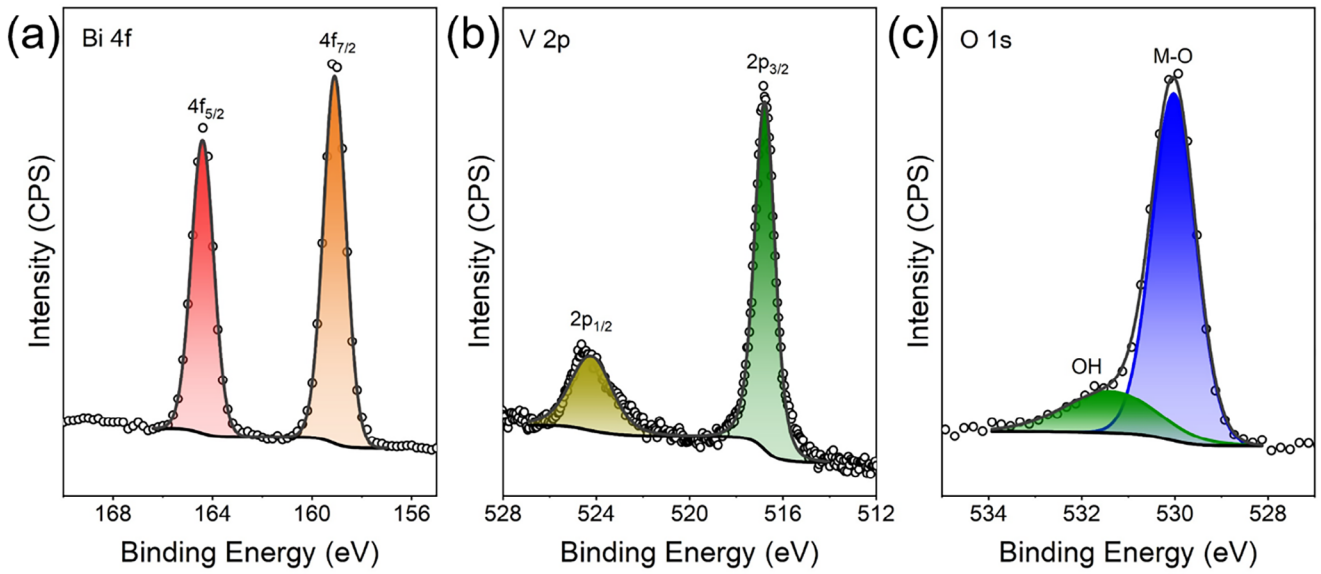

Figure 5. XPS spectra of a prototypical $BiVO_4$ photoanode prepared by Autodrop: a) Bi 4f b) V 2p c) O 1s.

simulated sunlight (AM 1.5G). The linear sweep voltammetry (LSV) curves of the $BiVO_4$ photoanodes with varying parameters are shown in Figure 6. All fabricated photoanodes displayed no significant electrocatalytic activity in the dark (dashed lines). The onset potential for all samples was ≈0.75 V versus RHE. As the dropped volume increased from 0.5 to 2 mL, the photocurrent density improved from 0.6 to 0.77 mA cm^{-2} at 1.23 V versus RHE. However, beyond a dropped volume of 2 mL, the photocurrent density decreased. Changing the spinning speed during fabrication had minimal effect on the photocurrent (Figure 6b), with values ranging from 0.75 to 0.8 mA cm^{-2}, except at the lowest spinning speed of 20 rps, where poor macroscopic homogeneity in film formation likely resulted in a low photocurrent (0.4 mA cm^{-2}) (Figure S5, Supporting Information). As shown

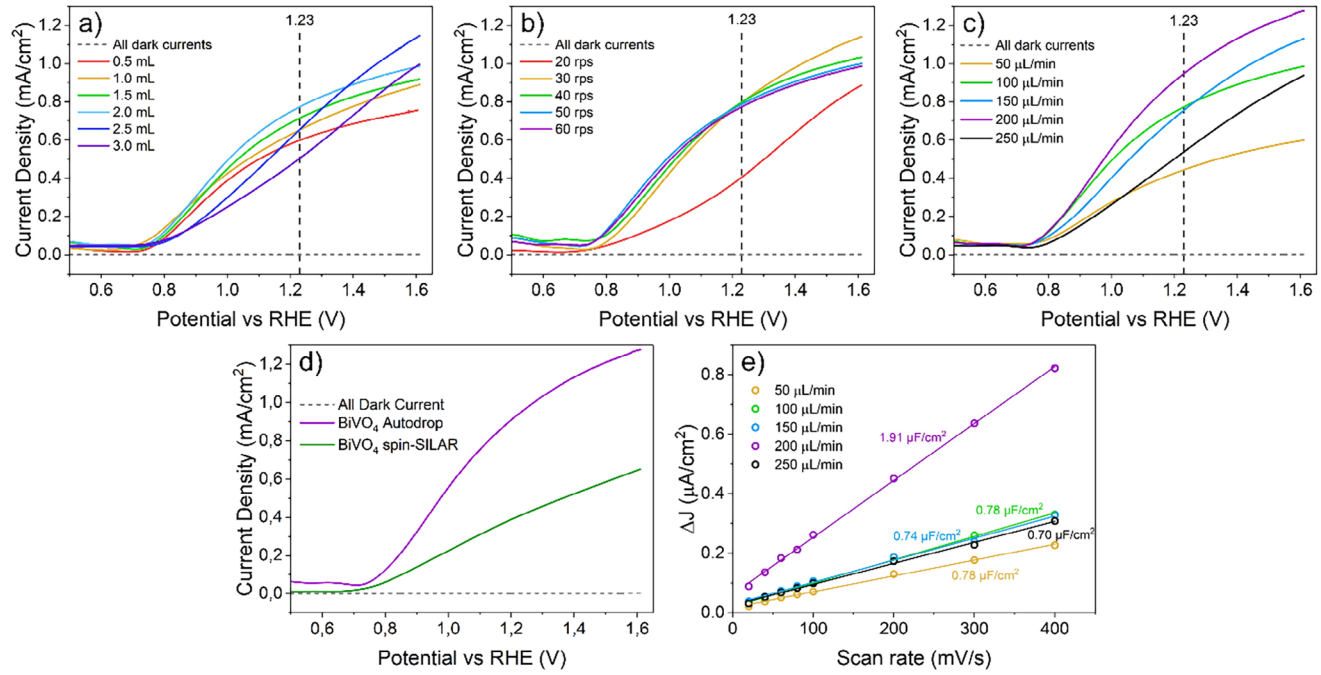

Figure 6. LSV data of the different series of $BiVO_4$ photoanodes prepared by Autodrop changing a) the dropped volume, b) the spinning speed, and c) the dropping rate. d) Best performing sample prepared via Autodrop compared with a spin-SILAR procedure e) Average current density ($\Delta J = (J_a - J_c)/2$) calculated at $\Delta E = 0.9$ V versus RHE against the scan rate, showing the C_{dl} of the samples prepared with different dropping rates, extracted from the cyclic voltammograms in Figure S7 (Supporting Information).

in the LSV curves in Figure 6c, the photocurrent increased with the dropping rate, reaching an optimized value of 0.95 mA cm^{-2} at 1.23 V versus RHE with 200 µL min^{-1}. A significant enhancement in photocurrent was noted as the dropping rate was adjusted. To understand this trend, the electrochemical surface area (ECSA) was analyzed and is presented in Figure 6e. The results indicate that the double-layer capacitance (C_{dl}) increases with the dropping rate, peaking at the sample with the highest photocurrent in Figure 6c. Beyond this optimal dropping rate, C_{dl} begins to decline. It is evident that the increase in photocurrent with rising bias is slower for the samples with dropping rates of 50 and 100 µL min^{-1} compared to the others. While the exact reason remains unclear, we hypothesize that at lower dropping rates, the resulting film thickness and porosity may be less favorable for efficient charge transfer, thereby hindering the kinetics of the OER in these samples. Based on these three sets of experiments, it is clear that the photocurrent can be significantly enhanced from 0.4 to 0.95 mA cm^{-2} by optimizing the experimental parameters. The optimal parameters for achieving the highest photocurrent in $BiVO_4$ films are 2 mL of precursor solution volume, 40 rps spinning speed, and a dropping rate of 200 µL min^{-1}. The performance of this sample was compared with a reference fabricated using the standard spin-SILAR method (see Experimental Section). The best-performing sample, produced via the Autodrop technique, exhibited a photocurrent more than twice that of the spin-SILAR sample (Figure 6d). This improvement is likely due to more efficient utilization of the precursors by Autodrop, as illustrated in Figure S6(Supporting Information). Although the microstructure of the films appears largely similar, the optical image in Figure S6a (Supporting Information) reveals that the spin-SILAR sample retains less material on the substrate than the optimized Autodrop sample (Figure S6b, Supporting Information), despite both using the same amount of precursors. These observations suggest that the Autodrop method enhances precursor utilization efficiency and minimizes material waste.

2.5. Characterization of $BiVO_4$—$FePO_4$ Photoanode

The optimized pure $BiVO_4$ film was further coated with an amorphous $FePO_4$ layer using the Autodrop method to enhance its efficiency and stability.[17] A thin $FePO_4$ film was first deposited on FTO and analyzed via XRD, which showed no characteristic peaks, indicating that the $FePO_4$ synthesized through the Autodrop method is amorphous (Figure S8, Supporting Information). Energy-dispersive X-ray (EDX) analysis confirmed the presence of Fe, P, V, and Bi in the composite film, as shown in **Figures** 7a–f and S9 (Supporting Information). SEM imaging of the surface revealed an irregular distribution of $FePO_4$, forming agglomerates that were distinctly visible in the EDX elemental maps of Fe and P. The atomic percentage ratio of Fe to P was measured at 54.6% and 45.4%, respectively, suggesting a slightly higher Fe concentration. Further characterization via X-ray photoelectron spectroscopy (XPS) confirmed the presence of Fe and P (Figure 7f–g; Figure S4c–4d, Supporting Information). In the Fe 2p region, two distinct peaks appeared at binding energies of 725.8 eV (Fe $2p_{1/2}$) and 712.0 eV (Fe $2p_{3/2}$), along with corresponding satellite peaks (Figure 7g). The observed spin-orbit splitting of 13.8 eV confirmed that Fe exists in the +3 oxidation state. The P 2p spectrum exhibited peaks at 134.0 eV (P $2p_{1/2}$) and 133.2 eV (P $2p_{3/2}$), confirming the presence of phosphate structures (Figure 7h).[26] The O 1s spectrum (Figure 7i) shows a main peak at binding energies of 531.4 eV, likely corresponding to O in the P—O bond, further supporting the presence of $FePO_4$.[17] The additional peak at lower binding energies (529.8 eV) can be assigned to bare $BiVO_4$, attributed to lattice O in $BiVO_4$, like for the pure material shown in Figure 5c. and the higher binding energy peak at 533.0 eV to hydroxide species adsorbed on the surface.

The PEC performance of the $BiVO_4$–$FePO_4$ photoanode fully prepared by Autodrop was evaluated and compared to that of pristine $BiVO_4$. Upon $FePO_4$ integration, the photocurrent density increased to 1.2 mA cm^{-2} at 1.23 V versus RHE, representing a ≈50% enhancement over the bare $BiVO_4$ (≈0.8 mA cm^{-2}), as confirmed by chopped-light LSV measurements (**Figure** 8b). The best-performing $BiVO_4$ and the corresponding $BiVO_4$–$FePO_4$ photoanodes were reproduced, and their PEC performance was evaluated under identical experimental conditions. The results demonstrated good reproducibility, as shown in Figure 8c, with photocurrent variations within ±10% at 1.23 V versus RHE. Regarding the chronoamperometry measurement, the pure $BiVO_4$ anode fails to maintain a stable photocurrent beyond 0.5 h. As shown in Figure S6c (Supporting Information), the morphology of the $BiVO_4$ film indicates no signs of mechanical damage. Therefore, the rapid decline in photocurrent is likely due to chemical or electrochemical degradation of the $BiVO_4$ material. A more significant improvement was observed in the stability of $BiVO_4$—$FePO_4$ anode: it retained over 80% of its initial photocurrent after ≈2 h of continuous operation, whereas the unmodified $BiVO_4$ showed a 50% loss within 20 min (Figure 8d). This exposure is likely responsible for the observed photocurrent decay after 2 h. Electrochemical impedance spectroscopy (EIS, Figure 8e) revealed a substantial reduction in charge transfer resistance (R_{ct}) after $FePO_4$ deposition, decreasing from 617 to 311 Ω, indicative of more efficient hole injection into the electrolyte. Mott–Schottky analysis (Figure 8f) confirmed typical n-type behavior for both samples. The flat band potential (V_{fb}) shifted from 0.02 to 0.12 V versus RHE upon $FePO_4$ integration, while the donor density (N_d) increased from 6.1×10^{18} cm^{-3} to 1.1×10^{19} cm^{-3}. We note that in a multilayer system such as $BiVO_4$–$FePO_4$, Mott–Schottky analysis primarily probes the properties of the outermost $FePO_4$ layer interfacing with the electrolyte, rather than those of the buried $BiVO_4$ layer alone. Therefore, the observed shift in flat band potential and increase in donor density should be interpreted as reflecting modifications at the interface, possibly due to improved band alignment or dipole formation, which reduce surface recombination and facilitate charge transfer. Similar approaches have been adopted in heterojunction systems to extract interfacial energetics and assess charge separation dynamics, even when the outer layer is not doped or crystalline.[27–29] These findings are consistent with the reduced charge transfer resistance observed by EIS (Figure 8e) and the enhanced photoelectrochemical performance. Incident photon-to-current conversion efficiency (IPCE) spectra (Figure 8g) further support this interfacial enhancement. The $BiVO_4$–$FePO_4$ fully Autodrop-fabricated photoanode exhibited a maximum IPCE of ≈20% at 425 nm, ≈1.6× higher than that of bare $BiVO_4$. The spectral response closely matched the UV–vis absorption profile (Figure 4), indicating that the photocurrent enhancement arises

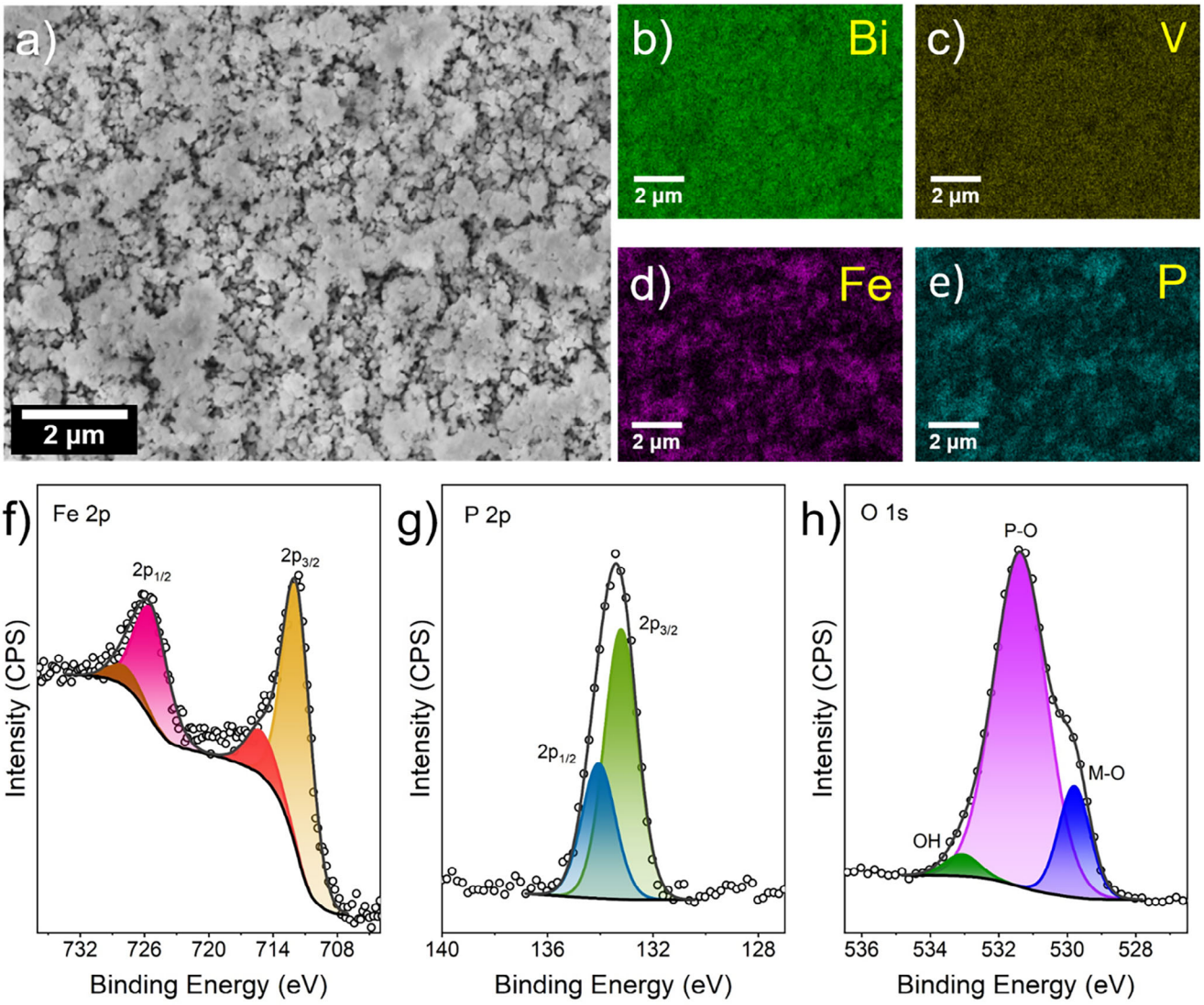

Figure 7. SEM-EDX analysis of a $BiVO_4$–$FePO_4$ thin film fully prepared by Autodrop: a) SEM image; b) Bi map; c) V map; d) Fe map; e) P map. XPS spectra of $BiVO_4$–$FePO_4$ f) Fe 2p g) P 2p h) O 1s.

primarily from improved interfacial charge dynamics rather than increased light absorption. These results confirm that $FePO_4$ acts as both a co-catalyst and a passivation layer, boosting PEC activity while significantly enhancing operational stability.

The proposed PEC-OER working mechanism for the $BiVO_4$–$FePO_4$ binary system is illustrated in **Figure 9**. Upon light irradiation, $BiVO_4$ absorbs photons, generating electron–hole pairs. Under an applied bias, the photogenerated electrons are transported through the conduction band to the FTO substrate and enter the external circuit, where they drive hydrogen evolution at the Pt cathode. However, some photocurrent is inevitably lost due to bulk recombination within the $BiVO_4$ layer. The introduction of $FePO_4$ mitigates these losses by enhancing interfacial charge separation and facilitating hole extraction. Although direct detection of reaction intermediates was not performed in this work, the proposed mechanism is based on extensive literature describing Fe-based phosphate catalysts. Specifically, Fe(III) sites in amorphous $FePO_4$ may efficiently scavenge photogenerated holes from $BiVO_4$ and be oxidized to Fe(IV)═O species—transient, high-valent intermediates widely recognized for their catalytic activity in water oxidation reactions.[30–32] These Fe(IV) species have been implicated in O—O bond formation steps, ultimately releasing O_2 and regenerating Fe(III). Operando studies on hematite have shown that the formation and consumption kinetics of Fe(IV)═O are tightly coupled to photocurrent generation, reinforcing their role in accelerating water oxidation kinetics.[33,34] In addition to this redox mediation, the phosphate matrix itself plays a synergistic role by anchoring the $FePO_4$ layer to the $BiVO_4$ surface and modulating interfacial charge transfer. Phosphate anions are known to displace surface hydroxyls on metal oxides, enhancing chemical bonding and stabilizing charge extraction pathways.[35,36] Such modifications have been shown to suppress recombination and improve the lifetime of photogenerated charges, especially in

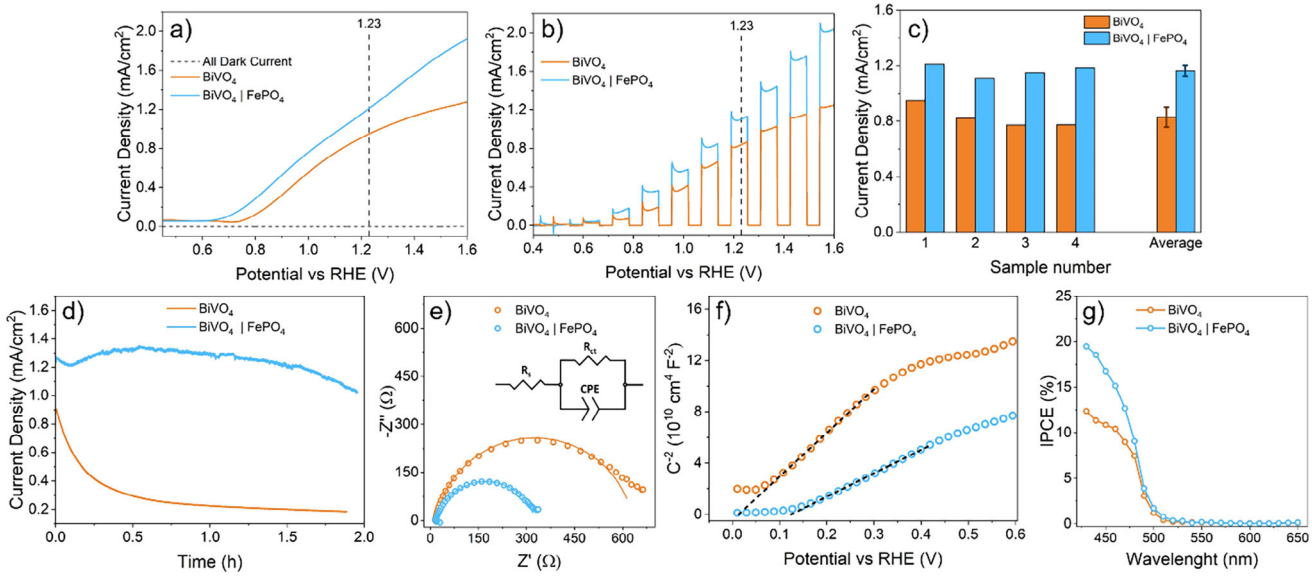

Figure 8. a) LSV, b) LSVs under chopped light, and c) Current density values at 1.23 V versus RHE from graphs in Figure S10 (Supporting Information), including average and standard deviation. The samples are not reported in a specific order. d) Chronoamperometry under simulated solar light. e) Nyquist plot under AM 1.5 G solar simulated light, f) Mott–Schottky plot (measured in dark), and g) IPCE of fully Autodrp-fabricated $BiVO_4$ thin films with and without a $FePO_4$ coating layer.

phosphate-functionalized oxides like TiO_2. Altogether, the enhancement observed in the $BiVO_4$–$FePO_4$ system can be interpreted as the result of a cooperative mechanism: Fe(III)/Fe(IV) redox cycling facilitates hole transfer and OER catalysis, while phosphate groups stabilize the interface and promote charge transport. This dual function—serving as both a passivation layer and a redox-active co-catalyst—provides a rational explanation for the improved performance and durability observed, although further operando spectroscopic studies would be needed to definitively confirm this mechanism.

3. Conclusion

In this study, we developed $BiVO_4$–$FePO_4$ photoanodes using a fully automated, aqueous-based deposition method ("Autodrop") that combines continuous precursor delivery with spin-assisted film formation. This scalable, low-temperature process enables precise control over film morphology and composition using water-based inks, offering a sustainable alternative to conventional deposition methods. The integration of an amorphous $FePO_4$ top-layer via the same Autodrop platform significantly

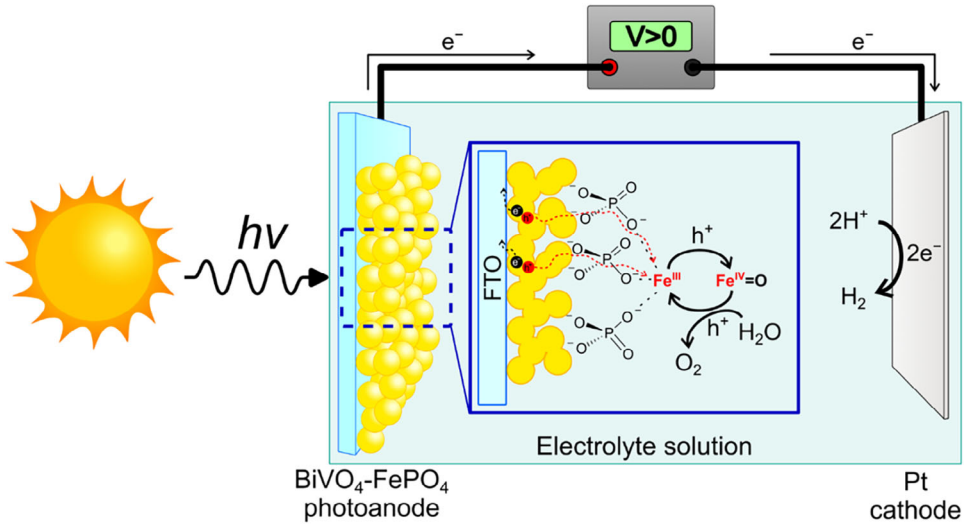

Figure 9. Proposed PEC-OER mechanism in $BiVO_4$–$FePO_4$ photoanodes. Photogenerated holes in $BiVO_4$ are extracted by Fe(III) sites, which may form transient Fe(IV)=O species catalyzing water oxidation. Phosphate groups enhance interfacial charge transfer. The mechanism is literature-based and not directly confirmed in this study.

enhanced both the photocurrent and operational stability of the $BiVO_4$ photoanodes. In particular, the modified electrodes achieved a 50% increase in photocurrent and retained over 80% of their initial activity after 2 h of continuous operation under AM 1.5G illumination at 1.23 V versus RHE. Mechanistic insights indicate that $FePO_4$ serves a dual role as a passivation layer and redox-active co-catalyst, facilitating hole transfer and suppressing surface recombination.

Beyond the specific $BiVO_4$–$FePO_4$ system, this work establishes Autodrop as a versatile platform for the fabrication of multilayer, functional semiconductor architectures under ambient conditions. Its compatibility with scalable, sustainable processing makes it a promising strategy for next-generation photoelectrode manufacturing and other solution-processed optoelectronic devices.

4. Experimental Section

Materials: Bismuth(III) nitrate pentahydrate ($Bi(NO_3)_3{\cdot}5H_2O$), ammonium vanadate (NH_4VO_3), sodium dihydrogen phosphate (NaH_2PO_4), and iron chloride ($FeCl_3$) were purchased from Thermo Fisher. FTO-coated glass substrates were purchased from Sigma–Aldrich.

Synthesis of Photoelectrodes: For $BiVO_4$, aqueous precursor solutions used were 5 mM NH_4VO_3 and 5 mM $Bi(NO_3)_3{\cdot}5H_2O$. It is important to prepare the $Bi(NO_3)_3$ solution immediately before use because $Bi(NO_3)_3$ can undergo hydrolysis over time, forming insoluble basic salts like $BiONO_3$, $Bi_2O_2(OH)NO_3$, and $Bi_6O_4(OH)_4(NO_3)_6{\cdot}H_2O$, which can affect the stoichiometry of the Bi precursor. The two solutions were simultaneously dispensed, using a Harvard Apparatus-11 Plus 70–2212 Syringe Pump, on the FTO substrate, which was continuously spun by a KLM Spin-Coater SCV-10. The solution was dispensed, having the droplets falling in an alternate way and not synchronously. The deposition time depended on the dropping rate and the total volume dropped. So, for example, dispensing 2.0 mL of the precursor solutions, the deposition time ranged from 80 min for the slowest rate used (25 µL min^{-1}) to 10 min for the fastest (200 µL min^{-1}). After deposition, the substrates were annealed at 450 °C for 2 h with a heating ramp of 10 °C min^{-1}. For $FePO_4$, the precursor solutions used were 25 mM $FeCl_3$ and 25 mM NaH_2PO_4 in aqueous form. The procedure was the same adopted for $BiVO_4$, and the parameters used were 100 µL min^{-1}, 40 rps, and 0.4 mL. The reference spin-SILAR sample was prepared using $Bi(NO_3)_3$ and NH_4VO4_3 solutions at the same concentrations as those used for the other samples. Each deposition cycle, performed manually, consisted of spinning 50 µL of the $Bi(NO_3)_3$ solution at 40 rps, followed by an identical step with the NH_4VO_3 solution. In total, 40 deposition cycles were carried out to fabricate the reference sample. The sample was then subjected to an annealing process under the same conditions used for the other $BiVO_4$ films. The substrate area coated with the active material was 1×1 cm^2 for all tested samples. A 2×2 cm^2 $BiVO_4$ prepared with the same parameters as the best-performing sample showed similar thickness compared with the 1×1 cm^2 sample (Figure S11, Supporting Information). Samples with an area larger than 2×2 cm^2 were not prepared due to the size limitation of a photoanode in the lab-scale electrochemical cell.

Characterizations: GIXRD measurements were performed on an Anton Paar XRDynamic 500 instrument using a Primux 3000 Cu Kα radiation ($\lambda = 1.5406$ Å) and a Pixos 2000 Detector. The instrument operated at a current of 45 mA and an acceleration voltage of 40 kV. SEM images were acquired using a Carl Zeiss GeminiSEM 560 field emission scanning electron microscope equipped with an InLens SE Detector. Imaging was conducted at an acceleration voltage of 3.00 kV, with a working distance of 3 mm, and a beam current of 100 pA. Optical absorption measurements in the UV–vis region were obtained using an Agilent Cary 5000 device equipped with an integrating sphere. XPS analysis was carried out on a PHI 5000 VersaProbe II Scanning ESCA Microprobe (Physical Electronics) equipped with a monochromatized Al Kα X-ray source operating in high power mode (beam size 1300 × 100 µm, X-ray power: 100 W). Spectra were acquired with time steps of 50 ms, a step size of 0.2 eV, and an analyzer pass energy of 46.95 eV. Each detailed region averaged over 30 sweeps or a P/N ratio of 180. The sample surface was neutralized using slow electrons and argon ions, and the measurement was conducted under vacuum conditions ranging from 10^{-7} Pa to 10^{-6} Pa. Data analysis was performed using CasaXPS software.

Photoelectrochemical Characterization: For the PEC measurements, a SP-300 potentiostat/galvanostat from BioLogic, controlled by EC-Lab software, was utilized. 0.5 M Na_2SO_4 aqueous solution at pH 7 was used as electrolyte for all the PEC characterizations. The setup employed a three-electrode configuration comprising a platinum wire counter electrode, an Ag/AgCl (saturated KCl) reference electrode, and a working electrode. Potentials recorded against Ag/AgCl were converted to the RHE scale using the equation:

$$E\ (V\ vs\ RHE) = E\ (V\ vs\ Ag/AgCl) + 0.197\ V + 0.059\ V \times pH \quad (1)$$

The working electrode consisted of an FTO-coated glass substrate, with half of it masked by an adhesive strip to form the multilayer photoelectrode only on one side. The masked part with bare FTO was connected to a platinum plate electrode holder. The samples were illuminated from the back with simulated solar light generated by an LS0106 Xenon arc lamp equipped with an LSZ189 AM 1.5G filter, and adjusted to an intensity of 100 mW cm^{-2} by use of a calibrated Si photodiode.

EIS was conducted at 1.23 V versus RHE under simulated solar light, sweeping frequencies from 100 kHz to 1 Hz.

Mott–Schottky measurements were performed in the dark within a voltage range of 0–0.6 V versus RHE (20 mV increments, 1 kHz frequency) to determine the flat band potential (V_{fb}) and the donor density (N_d). V_{fb} can be obtained from the intercept of the linear fit with the X axis, so when $1/C_2 = 0$, while N_d can be obtained from the slope $d(1/C_2)/dV$ using the formula:

$$N_d = \left(\frac{2}{A^2 e \epsilon \epsilon_0}\right)\left(\frac{1}{\frac{d\frac{1}{C^2}}{dV}}\right) \quad (2)$$

where A is the area of the electrode, e is the electron charge, ϵ is the dielectric constant for $BiVO_4$ ϵ_0 is the permittivity in vacuum.

C_{dl} was calculated from cyclic voltammetry (CVs) data using the equation:

$$C_{dl} = \frac{\Delta j}{2\upsilon} = \frac{j_a - j_c}{2\upsilon} \quad (3)$$

where j_a and j_c represent the anodic and cathodic current densities at a specific potential, and ν is the scan rate in mV s^{-1}. The ECSA can be estimated using the equation:

$$ECSA = \frac{C_{dl}}{C_s} \quad (4)$$

where C_s is the specific capacitance of the electrode, which corresponds to the capacitance of the material with a total actual surface of 1 cm^2.

The incident-photon-to-current conversion efficiency (IPCE) of the $BiVO_4$-based photoelectrode was evaluated using a potentiostat from Zahner Elektrik with an integrated lamp and monochromator in the CIMPS-QE/IPCE system. Measurements were conducted at 1.23 V versus RHE. The power density at each wavelength was determined based on the IPCE value of a standard silicon diode.

Supporting Information

Supporting Information is available from the Wiley Online Library or from the author.

Acknowledgements

T.G. acknowledges the support of the European Research Council for the project JANUS BI (Grant No. 101041229). M.W. and T.G. also thank Fondazione Compagnia di San Paolo for financial support through the "Bando TRAPEZIO – Paving the way to research excellence and talent attraction". T.G. is also further grateful to Compagnia di San Paolo for the support through the Starting Grant ERC program. R.A., B.S. and T.G. would like to thank the DFG for project 460609161.

Conflict of Interest

The authors declare no conflict of interest.

Author Contributions

R.A. performed data curation, conceptualization, visualization, investigation, and wrote the original draft. M.C. performed the investigation. B.S. gathered resources. D.S. gathered resources, wrote, reviewed, and edited the final manuscript. F.L. wrote, reviewed, and edited the final manuscript. T.G. performed supervision, project administration, and data curation, wrote, reviewed, and edited the final manuscript. M.W. performed data curation, wrote, reviewed, and edited the final manuscript.

Data Availability Statement

The data that support the findings of this study are available from the corresponding author upon reasonable request.

Keywords

automated SILAR, $BiVO_4$, photoanodes, solution processing

Received: March 29, 2025
Revised: June 25, 2025
Published online: July 9, 2025

[1] M. Noussan, P. P. Raimondi, R. Scita, M. Hafner, *Sustainability* **2021**, *13*, 298.
[2] G. Squadrito, G. Maggio, A. Nicita, *Renew Energy* **2023**, *216*, 119041.
[3] D. Gielen, E. Taibi, R. Miranda, *Hydrogen: A Reviewable Energy Perspective*, International Renewable Energy Agency (IRENA), Abu Dhabi **2019**.
[4] A. Vilanova, P. Dias, T. Lopes, A. Mendes, *Chem. Soc. Rev.* **2024**, *53*, 2388.
[5] A. Eftekhari, V. J. Babu, S. Ramakrishna, *Int. J. Hydrogen Energy* **2017**, *42*, 11078.
[6] Y. H. Lui, B. Zhang, S. Hu, *Front Phys (Beijing)* **2019**, *14*, 53402.
[7] J. K. Cooper, S. Gul, F. M. Toma, L. Chen, Y. S. Liu, J. Guo, J. W. Ager, J. Yano, I. D. Sharp, *J. Phys. Chem. C* **2015**, *119*, 2969.
[8] J. H. Kim, J. S. Lee, *Adv. Mater.* **2019**, *31*, 1806938.
[9] F. F. Abdi, T. J. Savenije, M. M. May, B. Dam, R. Van De Krol, *J. Phys. Chem. Lett.* **2013**, *4*, 2752.
[10] A. J. E. Rettie, H. C. Lee, L. G. Marshall, J. F. Lin, C. Capan, J. Lindemuth, J. S. McCloy, J. Zhou, A. J. Bard, C. B. Mullins, *J. Am. Chem. Soc.* **2013**, *135*, 11389.
[11] A. Kafizas, X. Xing, S. Selim, C. A. Mesa, Y. Ma, C. Burgess, M. A. McLachlan, J. R. Durrant, *Catal. Today* **2019**, *321*, 59.
[12] T. Moehl, J. Suh, L. Sévery, R. Wick-Joliat, S. D. Tilley, *ACS Appl. Mater. Interfaces* **2017**, *9*, 43614.
[13] L. Meng, W. Tian, F. Wu, F. Cao, L. Li, *J. Mater. Sci. Technol.* **2019**, *35*, 1740.
[14] M.-W. Kim, K. Kim, T. Yoon Ohm, H. Yoon, B. Joshi, E. Samuel, M. T. Swihart, S. K. Choi, H. Park, S. S. Yoon, *Chem. Eng. J.* **2017**, *333*, 721.
[15] A. Wang, D. Cao, F. Zhang, Y. Chen, J. Feng, D. Fang, B. Mi, Z. Gao, Z. Li, *ACS Catal.* **2024**, *14*, 3446.
[16] F. Parveh, A. Yourdkhani, R. Poursalehi, *New J. Chem.* **2023**, *47*, 15588.
[17] T.-G. Vo, Y. Tai, C.-Y. Chiang, *Appl. Catal. B* **2019**, *243*, 657.
[18] D. He, Q. Wang, W. Zhang, X. Liu, X. Cui, *ChemPhotoChem* **2023**, *7*, 202300080.
[19] A. Wang, Y. Chen, X. Liu, R. Li, Z. Zhang, F. Zhang, D. Cao, Z. Gao, B. Mi, *ACS Appl. Mater. Interfaces* **2025**, *17*, 12064.
[20] S. Wang, K. Wan, J. Feng, Y. Yang, S. Wang, *J. Mater. Sci. Technol.* **2025**, *217*, 182.
[21] S. P. Ratnayake, J. Ren, E. Colusso, M. Guglielmi, A. Martucci, E. D. Gaspera, *Small* **2021**, *17*, 2101666.
[22] W. Guo, D. Tang, O. Mabayoje, B. R. Wygant, P. Xiao, Y. Zhang, C. B. Mullins, *J. Electrochem. Soc.* **2017**, *164*, H119.
[23] S. P. Ratnayake, J. Ren, J. van Embden, C. F. McConville, E. D. Gaspera, *J Mater Chem A Mater* **2021**, *9*, 25641.
[24] R. Altieri, F. Schmitz, M. Schenker, F. Boll, L. Rebecchi, P. Schweitzer, M. Crisci, I. Kriegel, B. Smarsly, D. Schlettwein, F. Lamberti, T. Gatti, M. Wang, *Energy Adv.* **2024**, *3*, 2564.
[25] L. Chen, E. Alarcón-Lladó, M. Hettick, I. D. Sharp, Y. Lin, A. Javey, J. W. Ager, *J. Phys. Chem. C* **2013**, *117*, 21635.
[26] J. F. Moulder, W. F. Stickle, P. E. Sobol, K. D. Bomben, J. Chastain, in *Handbook of X-Ray Photoelectron Spectroscopy: A Reference Book of Standard Spectra for Identification and Interpretation of XPS Data*, (Ed: J. Chastain), Perkin-Elmer Corporation, Waltham **1992**.
[27] O. Almora, C. Aranda, E. Mas-Marzá, G. Garcia-Belmonte, A. P. Lett, *Appl. Phys. Lett* **2016**, *109*, 173903.
[28] K. Jeong, P. R. Deshmukh, J. Park, Y. Sohn, W. G. Shin, *ACS Sustain. Chem. Eng.* **2018**, *6*, 6518.
[29] J. He, S. Chen, Z. Ma, M. Wang, Q. He, *ACS Nano* **2024**, *18*, 24283.
[30] G. Righi, J. Plescher, F. P. Schmidt, R. K. Campen, S. Fabris, A. Knop-Gericke, R. Schlögl, T. E. Jones, D. Teschner, S. Piccinin, *Nat. Catal.* **2022**, *5*, 888.
[31] H.-C. Zhang, P.-X. Cui, D.-H. Xie, Y.-J. Wang, P. Wang, G.-P. Sheng, H.-C. Zhang, D.-H. Xie, G.-P. Sheng, P. Wang, P.-X. Cui, Y.-J. Wang, *Adv. Sci.* **2023**, *10*, 2205681.
[32] O. Zandi, T. W. Hamann, *Nat. Chem.* **2016**, *8*, 778.
[33] N. Yatom, O. Neufeld, M. Caspary Toroker, *J. Phys. Chem. C* **2015**, *119*, 24789.
[34] D. Li, R. Wei, F. Sun, Z. Cheng, H. Yin, F. Fan, X. Wang, C. Li, *J. Phys. Chem. Lett.* **2023**, *14*, 8069.
[35] C. Castañeda, K. Gutiérrez, I. Alvarado, J. J. Martínez, H. Rojas, F. Tzompantzi, R. Gómez, *J. Chem. Technol. Biotechnol.* **2020**, *95*, 3213.
[36] C. Castañeda, F. Tzompantzi, R. Gómez, H. Rojas, *J. Chem. Technol. Biotechnol.* **2016**, *91*, 2170.